

Efficient Hyperspectral Reconstruction from Wideband Images Based on Linear Mixing Model

M.Amine Hadj-Youcef, François Orieux, Alain Abergel, Aurélia Fraysse

Abstract

The aim of this paper is to reconstruct an hyperspectral object having two spatial dimensions and one spectral one from a set of blurred multispectral images taken at different wide bands. This multispectral image suffers from two main degradations. First, the spatial resolution is limited due to the spatial convolution of the hyperspectral object with the spectral-variant response called PSF (Point Spread Function). Secondly, the images suffer from a lack of spectral information because of the detector integration over wide bands.

To address this ill-posed problem, we propose an original reconstruction approach comprising a joint instrument model for the degraded spectral images together with a linear mixing model representing the hyperspectral object by weighted known spectral components. The reconstruction is based on minimization of a convex objective function composed of a data fidelity and an edge-preserving regularization term. The solution is computed by a half-quadratic algorithm alternating the minimization of a quadratic and a separable problem. We show that even with a non-circulant observation model, the algorithm is efficient and fast thanks to non-iterative algorithm for the closed-form quadratic solution.

Several tests are performed on synthetic data for the reconstruction of an astrophysical hyperspectral object observed with the MIRI (Mid-InfraRed Instrument) imager on board the space telescope of the next decade JWST (James Webb Space Telescope)¹. The reconstruction results show a significant increase in spatial and spectral resolutions compared to state of the art, with a relative error below 5% at 30 dB. Our proposed algorithm allows us to recover the spectroscopic information contained in broadband spectral images, and also to provide spectral images with constant spatial resolution over the entire spectral range.

Index Terms

Inverse Problems. Multispectral Imaging. Hyperspectral Imaging. Deconvolution. Image Reconstruction

EDICS Category: 11-TEC-FOR, 9-TEC-RST

M-Amine. Hadj-Youcef, François Orieux and Aurélia Fraysse are with Laboratoire des Signaux et Systèmes, Univ. Paris-Sud, CNRS, CentraleSupélec, Université Paris-Saclay, 3 rue Joliot-Curie, 91 192 Gif-sur-Yvette, France. e-mail: hadjyoucef.amine@gmail.fr

Alain Abergel is with the Institut d'Astrophysique Spatiale, CNRS, UMR 8617, Univ. Paris-Sud, Université Paris-Saclay, Univ. Paris-Sud, 91405 Orsay, France.

Manuscript received ????, ??, 2019; revised ????, ??, 2019.

¹<https://www.jwst.nasa.gov/>

Efficient Hyperspectral Reconstruction from Wideband Images Based on Linear Mixing Model

I. INTRODUCTION

Multispectral imaging systems are used in many fields, e.g., astrophysics [1], remote sensing [2], medicine [3] or microscopy [4]. They produce multispectral images by observing a hyperspectral ($2D+\lambda$) object. Depending on the wavelength, these images generally suffer from several undesirable spatial and spectral degradations. The spatial resolution is limited because of a 2D convolution of the hyperspectral object with the spectrally varying optical response or PSF (in particular for diffraction-limited imaging systems). Hence, the images are blurred. In addition, spectral information is lacking because of the detector integration over wide bands. The effects of these degradations become more important as the spectral range of observation is wide and the imaging system comprises only a few wide bands.

In this paper we address the hyperspectral reconstruction by joint spectral images processing, measured for different spectral bands, combined thanks to an inverse problem and a variational approach.

The state-of-the-art approach generally neglects the spectral variation of the PSF within a band [5], the reconstruction becoming an independent 2D deconvolution of multichannel images [6]. This method remains limited to systems with narrow spectral bands, which is generally not the case for multispectral imaging systems. Other works focus on the variability of the PSF especially for image deconvolution such as [7], [8], where the shift-variant PSF is approximated with a linearly interpolated PSF. Another technique, often used for astronomical images (e.g., [9], [10]) is the PSF homogenization between images obtained from different spectral bands or instruments. It consists of convolving the images with the appropriate kernel such that they appear as if they were measured with the same band or instrument. This approach is straightforward and simple, however, it introduces an additional blur and does not allow spectral reconstruction.

In [11] we proposed an instrument model to reproduce the degraded multispectral images with a piece-wise linear function chosen in order to model the spectral distribution. The proposed method presents some limitations, such as the tuning of the number of spectral samples. This parameter also represents the number of monochromatic images to reconstruct, i.e., the higher the value, the more ill-conditioned is the observation matrix. In addition, the algorithm is computationally expensive and time-consuming because of the iterative computation of the solution by a conjugate gradient algorithm.

The linear mixing/unmixing model is used to analyze hyperspectral data in [12]–[14]. It was first proposed in [15] for multispectral images, and since then it has been used in several applications [14], [16]–[18]. Some works consider the spatial and spectral correlations between neighboring pixels in order to analyze the hyperspectral data.

For instance, [19] proposed a spectral–spatial classification scheme for hyperspectral images, whereas [20] presented a hyperspectral image enhancement method based on the total variation. A Bayesian method for the extraction of end-members and the estimation of abundances from hyperspectral images has been proposed in [21]. A recent work in [22] proposed a comparison of several pansharpening techniques that are used for multispectral images and adapted for hyperspectral images.

In this paper we propose to use the linear mixing model for multispectral data (with a few wide bands) rather than hyperspectral data. Our approach consists of representing the hyperspectral object by a dictionary of M spectral components, assumed to be known, weighted by mixing coefficients to be estimated. The particularity of this method lies in the forward model. It accounts degradations modeling, object representation and joint processing of all wideband images at different bands. An efficient reconstruction based on variational methods [23] is developed, where the mixing coefficients are estimated by minimizing a convex objective function comprising a non-quadratic multichannel regularization term. The proposed algorithm is tested for the reconstruction of three different hyperspectral objects, one is a modeled astrophysical object and the other ones are synthetic objects allowing a better evaluation of the algorithm. The results clearly show a strong improvement in spectral and spatial resolution in comparison to the state of the art. The imaging system considered for this application is the Mid-InfraRed Instrument (MIRI) imager [24] on board the future James Webb Space Telescope (JWST) [25], which will be from 2021 the most ambitious telescope ever launched in space (largest primary mirror, highest spatial resolution and sensitivity ever achieved in the infrared, widest combination of imagers and spectrometers).

The paper is organized as follows. Section II presents the proposed methodology, first the instrument model developed for the imaging system (Section II-A), then the object representation model based on the linear mixing model (Section II-B) and finally the forward model (Section II-C). A reconstruction based on regularization methods is presented in Section III. Reconstruction results and discussions are presented in Section IV for the MIRI imager of the JWST. Finally, we conclude our work and provide perspectives in Section V.

II. PROPOSED METHODOLOGY

A. Instrument Model for the Imaging System

The hyperspectral object of interest is defined by

$$\phi(x, y, \lambda) : \mathbb{R}^2 \times \mathbb{R}_+ \rightarrow \mathbb{R}$$

where $(x, y) \in \mathbb{R}^2$ represent the spatial dimensions and $\lambda \in \mathbb{R}_+$ represents the spectral one. The imaging system consists of an optical system, a spectral filter, and a detector. The optical system response is carried out by a 2D convolution [26] between the hyperspectral object ϕ and the spectral-variant PSF, h , assumed to be known, $\iint_{\mathbb{R}^2} \phi(x', y', \lambda) h(x - x', y - y', \lambda) dx' dy'$. Hence, the object at the output of the optical system is blurred by a non-stationary PSF that depends on the wavelength λ which limits the spatial resolution of the images.

The blurred object is spectrally filtered over P wide spectral bands $\omega_p(\lambda)$, $p = 1, \dots, P$. Then the object is integrated within each band and sampled pixel-by-pixel on the detector matrix forming a discrete spectral image.

Therefore spectroscopic information of the hyperspectral object is reduced to only P discrete values. This represents a severe degradation of the hyperspectral object since P is usually a small number.

Spatial sampling at the pixel (i, j) corresponds to integration after multiplication by b_{samp} on a two-dimensional sampling grid $\mathcal{G}_{\text{samp}} = \{i\Delta_x, j\Delta_y\}_{i,j=1}^{N_i; N_j}$ where $N_{i,j}$ and $\Delta_{x,y}$ are the number of pixels and the spatial sampling steps along x and y , respectively. An additive term $n_{i,j}^p$ is added to the data to account for the detector noise. Finally, the complete equation of the imaging system model is given by

$$g_{i,j}^p = \iiint \iint \phi(x', y', \lambda) h(x - x', y - y', \lambda) dx' dy' \\ \omega_p(\lambda) b_{\text{samp}}(x - i\Delta_x, y - j\Delta_y) dx dy d\lambda + n_{i,j}^p. \quad (1)$$

The model in (1) establishes a relation between the continuous hyperspectral object ϕ and the discrete images $g^p, p = 1, \dots, P$ through the instrument response. It includes a spectral windowing and five sums for spatial convolution and spatio-spectral sampling.

B. Object Representation: Linear Mixing Model

We use the linear mixing model of [15] to represent the continuous hyperspectral object in a low-dimension space and keeping high spectral resolution. Therefore, the object is represented by a sum of M high-resolution known spectral components, $s^m(\lambda), m = 1, \dots, M$, weighted by M mixing coefficients $f_{k,l}^m$ associated to each spatial position (k, l) . Hence the object is decomposed on a uniform function b_{rec} defined over a two-dimensional grid $\mathcal{G}_{\text{rec}} = \{k\Delta'_x, l\Delta'_y\}_{k,l=1}^{N_k; N_l}$, where $N_{k,l}$ and $\Delta'_{x,y}$ are the number of samples and the sampling steps according to dimensions x and y , respectively. This yields

$$\phi(x, y, \lambda) = \sum_{m,k,l=1}^{M, N_k, N_l} f_{k,l}^m b_{\text{rec}}(x - k\Delta'_x, y - l\Delta'_y) s^m(\lambda). \quad (2)$$

C. Forward Model

The forward model is obtained by substituting (2) in (1) yielding

$$g_{i,j}^p = \sum_{m=1}^M \sum_{k=1}^{N_k} \sum_{l=1}^{N_l} H_{i;j,k;l}^{p,m} f_{k,l}^m + n_{i,j}^p \quad (3)$$

with

$$H_{i;j,k;l}^{p,m} = \iint \left(\left(\int \omega_p(\lambda) h(x, y, \lambda) s^m(\lambda) d\lambda \right)_{x,y} * b_{\text{rec}}(x - k\Delta'_x, y - l\Delta'_y) \right) b_{\text{samp}}(x - i\Delta_x, y - j\Delta_y) dx dy, \quad (4)$$

where $*_{x,y}$ indicates the 2D convolution symbol.

In practice we set $\Delta'_x = \Delta_x$ and $\Delta'_y = \Delta_y$, and the spectral integration in (4) is computed numerically. The observation matrix becomes a numerical convolution matrix by setting b_{samp} and b_{rec} to rectangular functions, i.e., $H_{i;j,k;l}^{p,m} = H_{i-k,j-l}^{p,m}$. We end up with the matrix-vector representation of the forward model as follows

$$\mathbf{g}^p = \sum_{m=1}^M \mathbf{H}^{p,m} \mathbf{f}^m + \mathbf{n}^p, \quad p = 1, 2, \dots, P, \quad (5)$$

where the p -th image $\mathbf{g}^p \in \mathbb{R}^{N_i N_j}$ is a sum of M discrete spatial convolutions of mixing coefficients $\mathbf{f}^m \in \mathbb{R}^{N_k N_l}$, $m = 1, \dots, M$, with convolution matrix $\mathbf{H}^{p,m} \in \mathbb{R}^{N_i N_j \times N_k N_l}$, plus an additive noise $\mathbf{n}^p \in \mathbb{R}^{N_i N_j}$.

We propose to process the whole together in order to reconstruct the total spectral information of the hyperspectral cube, instead of a separable processing band per band [27]. This has the advantage of taking into account cross-correlations between images. Therefore, by concatenation of all images in one vector, it is natural to obtain the following multi-observations forward model

$$\mathbf{g} = \mathbf{H}\mathbf{f} + \mathbf{n}, \quad (6)$$

where $\mathbf{g}^T = [\mathbf{g}^1, \dots, \mathbf{g}^P]^T$, $\mathbf{f}^T = [\mathbf{f}^1, \dots, \mathbf{f}^M]^T$, and $\mathbf{n}^T = [\mathbf{n}^1, \dots, \mathbf{n}^P]^T$. The full system observation matrix

$$\mathbf{H} = \begin{bmatrix} \mathbf{H}^{1,1} & \dots & \mathbf{H}^{1,M} \\ \vdots & \ddots & \vdots \\ \mathbf{H}^{P,1} & \dots & \mathbf{H}^{P,M} \end{bmatrix}$$

is a non-square non-Toeplitz with Toeplitz blocks $\mathbf{H}^{p,m}$ representing the contribution of template m to images p . For computational efficiency, the convolutions are done in the Fourier domain [28] under the circular assumption.

III. HYPERSPECTRAL RECONSTRUCTION

A. Variational estimation

The problem defined in Eq. (6) is ill-posed due to the convolution involved. The common approach in that case is to add prior information about the solution for instance by regularized least square method [23]. Therefore, the solution $\hat{\mathbf{f}}$ is obtained as a minimizer of the objective function $\mathcal{J}(\mathbf{f})$

$$\hat{\mathbf{f}} = \underset{\mathbf{f}}{\operatorname{argmin}} \left\{ \mathcal{J}(\mathbf{f}) = \mathcal{Q}(\mathbf{f}, \mathbf{g}) + \mu \mathcal{R}(\mathbf{f}) \right\}, \quad (7)$$

where $\mathcal{Q}(\mathbf{f}, \mathbf{g})$ is a data fidelity term, $\mathcal{R}(\mathbf{f})$ a regularization term added to correct the ill-conditioning of the problem, and $\mu \geq 0$ a regularization parameter to tune the trade-off between both these terms.

The noise is chosen with an identically independent Gaussian distribution leading to $\mathcal{Q}(\mathbf{f}, \mathbf{g}) = \|\mathbf{g} - \mathbf{H}\mathbf{f}\|_2^2$. Concerning the regularization term, many possibilities have been explored in the literature. For instance, one can consider Tikhonov regularization [29], total variation [30], wavelet-domain regularization [31], [32], or half-quadratic regularization [33], [34]. Here we are interested in the reconstruction of a spatially smooth hyperspectral object. The prior information is then introduced by penalizing the horizontal and vertical differences between neighboring

pixels of each mixing coefficient. In that case, a multichannel regularization term is defined as

$$\mathcal{R}(\mathbf{f}) = \sum_{m,k,l=1}^{M,N_k,N_l} \varphi \underbrace{(\mathbf{f}_{k+1,l}^m - \mathbf{f}_{k,l}^m)}_{[\mathbf{D}_v \mathbf{f}^m]_{k,l}} + \varphi \underbrace{(\mathbf{f}_{k,l+1}^m - \mathbf{f}_{k,l}^m)}_{[\mathbf{D}_h \mathbf{f}^m]_{k,l}}, \quad (8)$$

where φ is the penalty function. \mathbf{D}_h and \mathbf{D}_v are first-order finite difference operators, with circularity conditions $f_{N_k+1,l}^m = f_{1,l}^m$ and $f_{k,N_l+1}^m = f_{k,1}^m$. A classical choice is the quadratic function $\varphi(x) = x^2$ that gives a differentiable objective function and an explicit solution. However, spatial sharp edges are smoothed.

To overcome this limitation we propose to use a non-quadratic penalty function. Several methods are found in the literature such as method based on partial differential equation [35], total variation (ℓ_1 -norm of the gradient) [30], [36] or half-quadratic regularization ($\ell_2\ell_1$ -norm) [33], [34], [37]. We are particularly interested in the method proposed in [34] for practical reasons. Firstly, the minimization of the objective function is done through alternating quadratic and separable minimization problems. Secondly, the quadratic solution is directly tractable thanks to the invert of the Hessian matrix in the Fourier domain. Thirdly, a variety of penalty functions can be used like the Huber function used in the rest of this work. The half-quadratic regularization proposed by *Geman & Yang* in [34] consists of introducing $N_k \times N_l$ horizontal and vertical *auxiliary* variables, b , such that the penalty function φ is expressed as the minimum wrt. b of the sum of a quadratic function $(x - b)^2/2$ and an auxiliary function $\xi(b)$

$$\varphi(x) = \inf_b \psi(b) = \inf_b \frac{1}{2}(x - b)^2 + \xi(b), \quad \forall x \in \mathbb{R}. \quad (9)$$

The role of the auxiliary variables can be seen as shifting the quadratic function to a suitable position such as the cost at high gradient values is lower compared to the cost of the quadratic regularization. The auxiliary function relies on the convex duality and Legendre-Fenchel transform [33], [34], [37], [38]. For instance, the auxiliary function associated to the Huber penalty is defined in [38] by

$$\xi(b) = a \begin{cases} \frac{1}{1-2a} b^2, & \text{if } |b| < (1-2a)s, \\ 2s|b| - (1-2a)s^2, & \text{otherwise,} \end{cases} \quad (10)$$

where $a \in [0, 1/2]$ is a scale parameter. Consequently, an augmented objective function \mathcal{J}^* is

$$\begin{aligned} \mathcal{J}^*(\mathbf{f}, \mathbf{b}_h, \mathbf{b}_v) = & \|\mathbf{g} - \mathbf{H}\mathbf{f}\|_2^2 + \frac{\mu}{a} \sum_{m=1}^M \left(\sum_{k,l=1}^{N_k, N_l} \right. \\ & \frac{1}{2} \left([\mathbf{D}_h \mathbf{f}^m]_{k,l} - [\mathbf{b}_h^m]_{k,l} \right)^2 + \xi([\mathbf{b}_h^m]_{k,l}) + \\ & \left. \frac{1}{2} \left([\mathbf{D}_v \mathbf{f}^m]_{k,l} - [\mathbf{b}_v^m]_{k,l} \right)^2 + \xi([\mathbf{b}_v^m]_{k,l}) \right) \end{aligned} \quad (11)$$

such that

$$\inf_{\mathbf{b}_h, \mathbf{b}_v} \mathcal{J}^*(\mathbf{f}, \mathbf{b}_h, \mathbf{b}_v) = \mathcal{J}(\mathbf{f}). \quad (12)$$

Here \mathbf{b}_h and \mathbf{b}_v are vector representations of the stack of auxiliary variables along the horizontal and vertical directions. Therefore, the multichannel half-quadratic solution is obtained by minimizing the augmented objective

function

$$\left(\hat{\mathbf{f}}, \hat{\mathbf{b}}_h, \hat{\mathbf{b}}_v \right) = \underset{\mathbf{f}, \mathbf{b}_h, \mathbf{b}_v}{\operatorname{argmin}} \mathcal{J}^*(\mathbf{f}, \mathbf{b}_h, \mathbf{b}_v). \quad (13)$$

The computation of the joint minimizer of $\mathcal{J}^*(\mathbf{f}, \mathbf{b}_h, \mathbf{b}_v)$ with respect to $(\mathbf{f}, \mathbf{b}_h, \mathbf{b}_v)$ is achieved by iterating a two stage process until convergence:

$$\left\{ \begin{array}{l} \hat{\mathbf{f}}^{(k)} = \underset{\mathbf{f}}{\operatorname{argmin}} \mathcal{J}^* \left(\mathbf{f}, \mathbf{b}_h^{(k-1)}, \mathbf{b}_v^{(k-1)} \right), \\ \hat{\mathbf{b}}_h^{(k)}, \hat{\mathbf{b}}_v^{(k)} = \underset{\mathbf{b}_h, \mathbf{b}_v}{\operatorname{argmin}} \mathcal{J}^* \left(\mathbf{f}^{(k)}, \mathbf{b}_h, \mathbf{b}_v \right). \end{array} \right. \quad (14)$$

$$\left\{ \begin{array}{l} \hat{\mathbf{f}}^{(k)} = \underset{\mathbf{f}}{\operatorname{argmin}} \mathcal{J}^* \left(\mathbf{f}, \mathbf{b}_h^{(k-1)}, \mathbf{b}_v^{(k-1)} \right), \\ \hat{\mathbf{b}}_h^{(k)}, \hat{\mathbf{b}}_v^{(k)} = \underset{\mathbf{b}_h, \mathbf{b}_v}{\operatorname{argmin}} \mathcal{J}^* \left(\mathbf{f}^{(k)}, \mathbf{b}_h, \mathbf{b}_v \right). \end{array} \right. \quad (15)$$

B. Computation of the mixing coefficients $\hat{\mathbf{f}}$

From (11) and (14) we have the quadratic criterion

$$\hat{\mathbf{f}} = \underset{\mathbf{f}}{\operatorname{argmin}} \left\{ \| \mathbf{g} - \mathbf{H} \mathbf{f} \|_2^2 + \frac{\mu}{2a} \left(\| \overline{\mathbf{D}}_h \mathbf{f} - \mathbf{b}_h \|_2^2 + \| \overline{\mathbf{D}}_v \mathbf{f} - \mathbf{b}_v \|_2^2 \right) \right\}, \quad (16)$$

with $\overline{\mathbf{D}} = \operatorname{diag}\{\mathbf{D}_1, \dots, \mathbf{D}_L\}$. The minimizer is explicit and is obtained by canceling the gradient. This yields

$$\hat{\mathbf{f}} = \underbrace{\left(\mathbf{H}^T \mathbf{H} + \mu' \left(\overline{\mathbf{D}}_h^T \overline{\mathbf{D}}_h + \overline{\mathbf{D}}_v^T \overline{\mathbf{D}}_v \right) \right)^{-1}}_{\mathbf{Q}} \underbrace{\left(\mathbf{H}^T \mathbf{g} + \mu' \left(\overline{\mathbf{D}}_h^T \mathbf{b}_h + \overline{\mathbf{D}}_v^T \mathbf{b}_v \right) \right)}_{\mathbf{q}}, \quad (17)$$

where the Hessian matrix $\mathbf{Q} \in \mathbb{R}^{MN_k N_l \times MN_k N_l}$ is a Non-Circulant Block Circulant matrix, $\mathbf{q} \in \mathbb{R}^{MN_k N_l}$ is a multichannel vector, and $\mu' = \mu/2a$.

A common computational approach of $\hat{\mathbf{f}}$ relies of solving the linear system $\mathbf{Q} \mathbf{f} = \mathbf{q}$ without requiring the inversion of \mathbf{Q} with an iterative algorithm, except in pure circulant deconvolution or small system. On the contrary, in this paper the solution is directly computed thanks to feasible inversion of \mathbf{Q} and fast Fourier transform as described in Appendix A. This approach is used in [39] and consists of assuming circularity of the block matrices, \mathbf{D}_h , \mathbf{D}_v and $\mathbf{H}^{p,m}$.

C. Update of the auxiliary variables $\hat{\mathbf{b}}_h, \hat{\mathbf{b}}_v$

From (11) and (15) we have

$$\hat{\mathbf{b}}_h, \hat{\mathbf{b}}_v = \underset{\mathbf{b}_h, \mathbf{b}_v}{\operatorname{argmin}} \sum_{m, k, l=1}^{M, N_k, N_l} \psi \left([\mathbf{b}_h]_{k, l} \right) + \psi \left([\mathbf{b}_v]_{k, l} \right) \quad (18)$$

where ψ is a convex and differentiable function. Moreover, the update equation for each auxiliary variable is explicit and separable with

$$\left[\hat{\mathbf{b}}_*^m \right]_{k, l} = \underset{[\mathbf{b}_*^m]_{k, l}}{\operatorname{argmin}} \psi \left([\mathbf{b}_*^m]_{k, l} \right). \quad (19)$$

The computation of the minimizers in (19) is straightforward and is given in Appendix B. Finally, we obtain

$$\hat{\mathbf{b}}_* = \overline{\mathbf{D}}_* \mathbf{f} - a \varphi' (\overline{\mathbf{D}}_* \mathbf{f}) \quad (20)$$

where φ' is the first derivative of the Huber function given by

$$\varphi'(x) = \begin{cases} 2x, & \text{if } |x| < s, \\ 2s \operatorname{sign}(x), & \text{otherwise.} \end{cases}$$

The proposed algorithm is summarized in a pseudo-algorithm form in Algorithm 1.

Algorithm 1 The Hyperspectral Reconstruction

Input: $\mathbf{H}, \mathbf{D}_h, \mathbf{D}_v, \mathbf{g}, \mu, a \in [0, 1/2]$

Initialization: $\hat{\mathbf{b}}_h = \hat{\mathbf{b}}_v = \mathbf{0}$

$\bar{\mathbf{F}} = \operatorname{diag}\{\mathbf{F}, \dots, \mathbf{F}\}$

$\bar{\mathbf{D}}_h = \operatorname{diag}\{\mathbf{D}_h, \dots, \mathbf{D}_h\}$

$\bar{\mathbf{D}}_v = \operatorname{diag}\{\mathbf{D}_v, \dots, \mathbf{D}_v\}$

Compute the Hessian matrix

$$\mathbf{Q} \leftarrow \mathbf{H}^T \mathbf{H} + \mu' (\bar{\mathbf{D}}_h^T \bar{\mathbf{D}}_h + \bar{\mathbf{D}}_v^T \bar{\mathbf{D}}_v)$$

Compute the inverse matrix Υ

$$\Upsilon \leftarrow \bar{\mathbf{F}}^\dagger \mathbf{Q}^{-1} \bar{\mathbf{F}}$$

▷ See Appendix A

while criterion is not reached **do**

 1 – Compute the solution (mixing coefficients)

$$\mathbf{q} \leftarrow \mathbf{H}^T \mathbf{g} + \frac{\mu}{2a} (\bar{\mathbf{D}}_h^T \hat{\mathbf{b}}_h + \bar{\mathbf{D}}_v^T \hat{\mathbf{b}}_v)$$

$$\hat{\mathbf{f}} \leftarrow \mathbf{Q}^{-1} \mathbf{q} = \bar{\mathbf{F}}^\dagger \Upsilon \bar{\mathbf{F}} \mathbf{q}$$

 2 – Update the auxiliary variables in parallel

$$\hat{\mathbf{b}}_h \leftarrow \bar{\mathbf{D}}_h \hat{\mathbf{f}} - a \varphi' (\bar{\mathbf{D}}_h \hat{\mathbf{f}})$$

$$\hat{\mathbf{b}}_v \leftarrow \bar{\mathbf{D}}_v \hat{\mathbf{f}} - a \varphi' (\bar{\mathbf{D}}_v \hat{\mathbf{f}})$$

end while

return $\hat{\mathbf{f}}$

IV. EXPERIMENTAL RESULTS

In this section we present tests and comparisons of the proposed algorithm for the reconstruction of three hyperspectral objects having different spatial and spectral distributions. One is a modeled astrophysical object and the other ones are synthetic objects. The imaging system we consider is the MIRI imager on board the JWST [25].

A. The MIRI Imager of the JWST

The optical system of the JWST is equipped with a 6.5 meters primary mirror composed of 18-hexagonal segments. The analytic expression of the PSF at one wavelength can theoretically be obtained by computing the Fourier transform of the transmittance of the telescope aperture, due to the diffraction theory [26]. To take into account misalignment of the 18 segments and the optical path differences (OPD), the PSFs are computed with *WebbPSF*

[40], [41], the official PSF simulator for the JWST developed by the Space Telescope Science Institute (STScI)². Fig. 1 display monochromatic PSFs computed at 6, 12, and 18 μm . We clearly see the spectral dependence of the PSF, i.e., the longer the wavelength the wider the PSF, according to diffraction theory.

The images are integrated over $P = 9$ spectral wide-bands covering a spectral range from 5 to 30 μm shown in Fig. 2. The MIRI imager provides images with a field of view of 74×113 arcsecond² using an infrared detector with a pixel scale of 0.11 arcsecond, i.e. a field of view per pixel of 0.11×0.11 arcsecond².

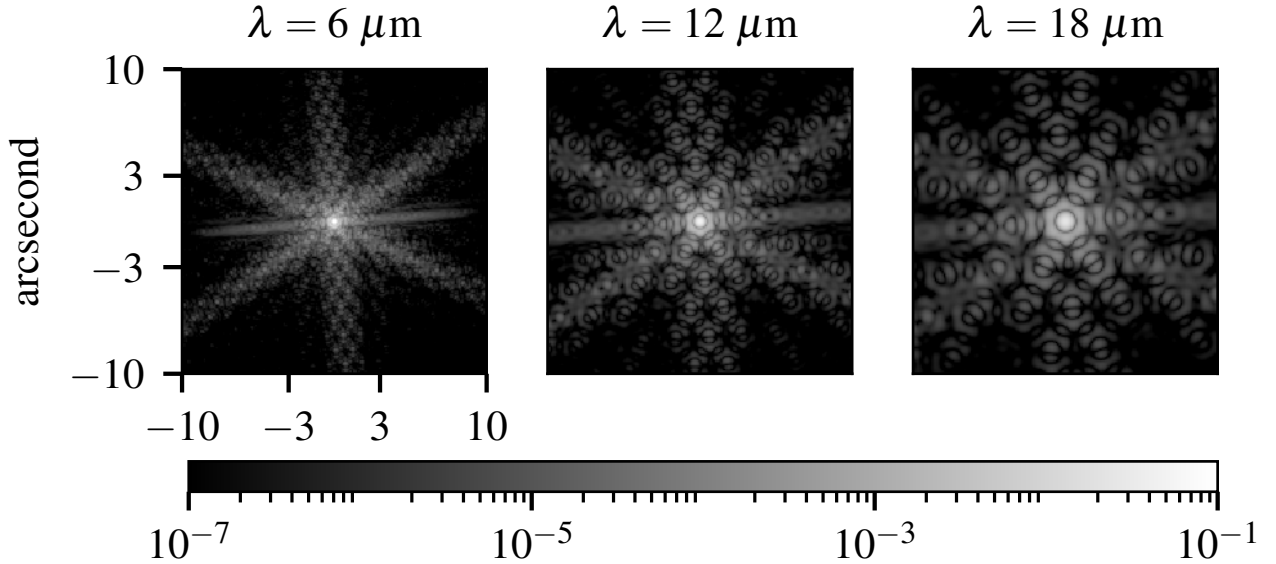


Fig. 1. Monochromatic PSF of the JWST/MIRI imager simulated using *WebbPSF* [40] displayed in logarithmic scale.

B. Description of the hyperspectral objects

The multispectral image is computed with equation (1) for three hyperspectral objects. The first one, denoted by Obj₁, is a simplified hyperspectral object of the *HorseHead nebula* [44], modeling a cloud of matter (dust and gas) illuminated by a bright star³, with $N_{k;l} = 256$ spatial samples, and $N_\lambda = 1000$ spectral samples uniformly distributed from 1 to 30 μm . For the reconstruction, M spectral components s^m are computed with PCA [45] from Obj₁. For that object only $M = 3$ components (shown in Fig. 3) are sufficient to explain 99.99% of the variance of the spectra. Note that other extraction techniques could be used such as the non-negative matrix factorization [46], or blind source separations [18], but this is not necessary in our case.

Two hyperspectral objects with more complex spatial and spectral distributions, Obj₂ and Obj₃, are synthesized. Fig. 4 and Fig. 5 display the spectral components and the original mixing coefficients used to synthesize Obj₂ and Obj₃, respectively. For both objects, the spectral components are taken from [18] and extracted from real data taken by the spectrometer of the *Spitzer* Space Telescope which covers the same spectral range as the MIRI imager. For the mixing coefficients of Obj₂ we take $M = 3$ rectangular patterns of different size with sharp edges, each

²<http://www.stsci.edu/>

³This 2D+ λ object has been computed using state-of-the-art interstellar dust models and radiative transfer codes.

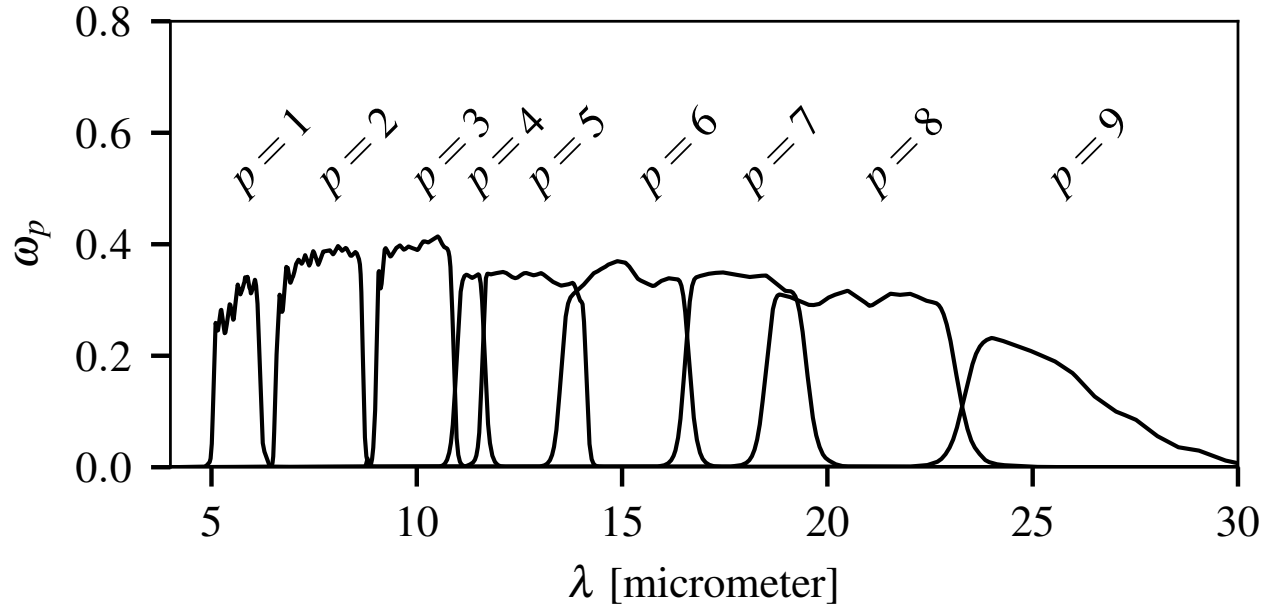


Fig. 2. Wide spectral bands of the JWST/MIRI Imager [42], from [43].

associated to one of the three spectral components. For Obj_3 we take $M = 2$ mixing coefficients in order to create a complex high-frequency spatial structure with a smooth horizontal gradient.

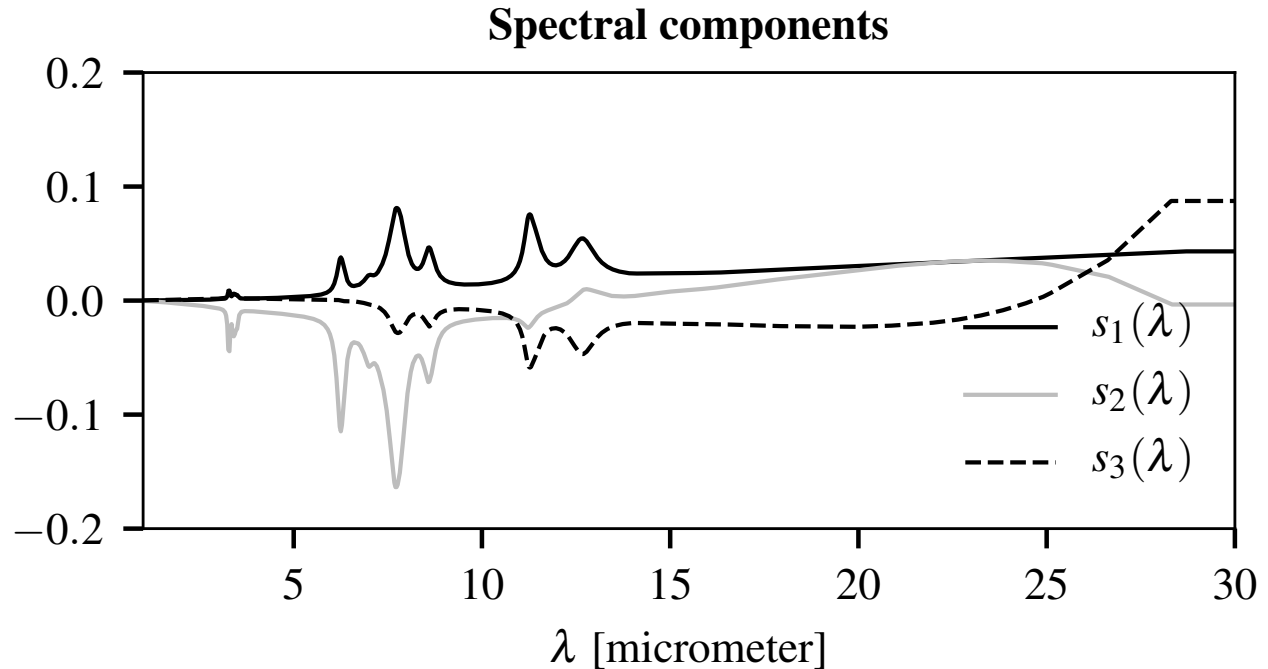


Fig. 3. Three spectral components extracted from Obj_1

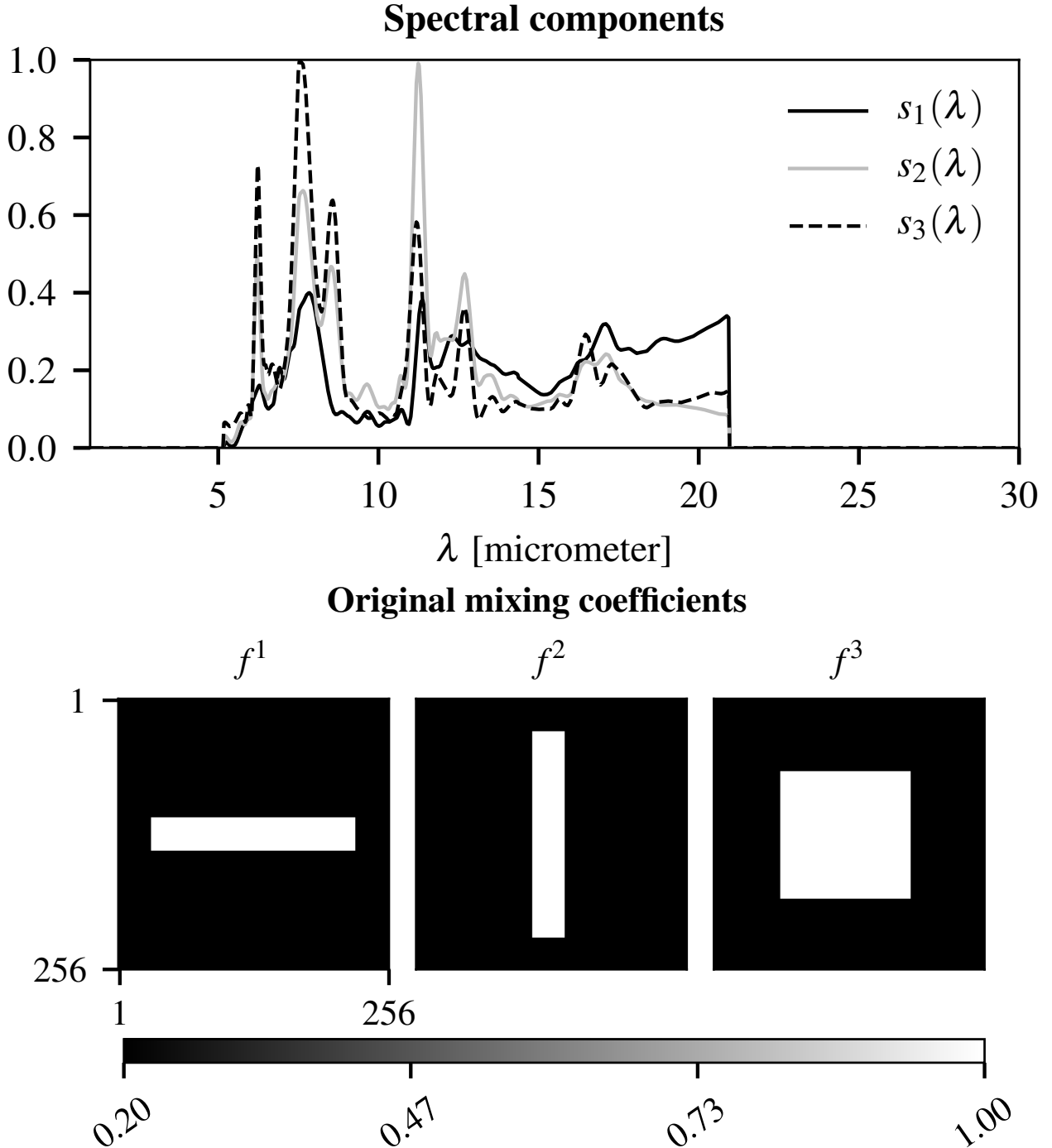


Fig. 4. Spectral components and mixing coefficients for Obj_2 .

C. Simulation of the multispectral data

The $P = 9$ images for Obj_1 , Obj_2 , and Obj_3 are simulated using the MIRI imager instrument model in (1). We degrade the images with an additive zero-mean, white, Gaussian noise of different levels of Signal-to-Noise Ratio (SNR), that is 5, 10, 20, 30, and 40 dB, defined as $\text{SNR} = 10 \log_{10} (\|\mathbf{g}\|_2^2 / N\sigma_n^2)$ where σ_n is the standard

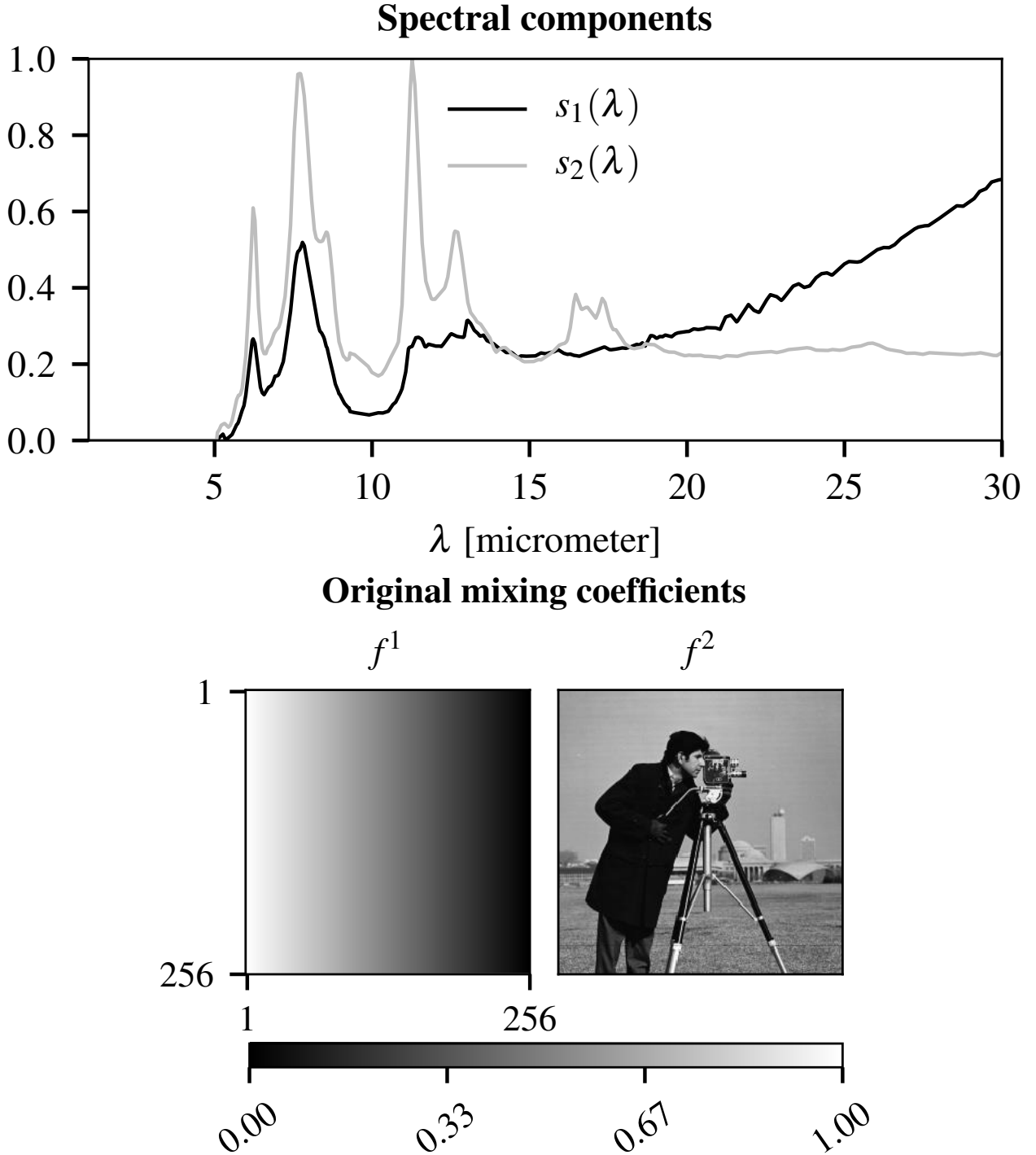


Fig. 5. Spectral components and mixing coefficients for Obj_3 .

deviation of the noise, and N is the total number of pixels in \mathbf{g} .

The simulated multispectral images with SNR = 30 dB and $p = 1, 4, 7$ are displayed in the first row of Figs. 8, 9, and 10, for Obj_1 , Obj_2 and Obj_3 , respectively, to illustrate the complexity of the imaging system. The blur increases for increasing wavelengths due to the convolution by a varying PSF in wavelength. The images have

TABLE I
RECONSTRUCTION ERRORS WITH 50 ITERATIONS.

Object	Error [%]	Runtime [s]	μ	s
$\widehat{\text{Obj}}_1$	0.67	22.02	5.99×10^{-2}	1.17
$\widehat{\text{Obj}}_2$	1.91	21.84	4.64×10^{-2}	0.03
$\widehat{\text{Obj}}_3$	4.91	21.84	5.99×10^{-2}	0.01

different intensities due to the spectral distribution integrated within the spectral bands and the width of each band. To sum up, the simulated images are heterogeneous, limited in spatial resolution and contain poor spectral information.

D. Estimation results of $\widehat{\mathbf{f}}$, $\widehat{\mathbf{b}}_h$ and $\widehat{\mathbf{b}}_v$

For the reconstruction, the parameters μ and s are chosen in order to minimize the reconstruction error (in %)

$$\text{Error}(\mu, s) = \|\mathbf{f}_{\text{orig}} - \mathbf{f}_{\text{rec}}(\mu, s)\|_2 / \|\mathbf{f}_{\text{orig}}\|_2 \times 100, \quad (21)$$

with values reported in Table I. The spatial distributions of the estimated mixing coefficients $\widehat{\mathbf{f}}$ are shown in Fig. 6. For Obj_1 we see in Fig. 6 (Top) that $\widehat{\mathbf{f}}^1$ has a higher intensity than $\widehat{\mathbf{f}}^2$ and $\widehat{\mathbf{f}}^3$, which is simply due to the domination of the first spectral component in the spectral distribution of Obj_1 . For Obj_2 and Obj_3 , Figs. 6 (Middle) and (Bottom) show that the mixing coefficients appear properly unmixed and deconvolved.

The spatial distributions of the estimated auxiliary variables $(\widehat{\mathbf{b}}_h, \widehat{\mathbf{b}}_v)$, shown in Fig. 7 for Obj_2 mimic the contours of the mixing coefficients, as expected from the half-quadratic minimization.

The proposed algorithm is coded using Python codes 2.7 and executed on a laptop machine with a memory of 16 GiB RAM and a processor Intel Core i7 CPU 2.50 GHz.

E. Hyperspectral Reconstruction Results

The reconstructed objects are computed using the linear mixing model in (2) and using the estimated coefficients presented above. In Table I we present the algorithm parameters and reconstruction errors for the three objects.

All reconstruction errors are below 5%. The smallest error (0.67%) is obtained for $\widehat{\text{Obj}}_1$ which presents no sharp edge neither complex spectral features. For $\widehat{\text{Obj}}_2$ and $\widehat{\text{Obj}}_3$, reconstruction errors are 1.91% and 4.91%, respectively, because of their more complex spatial and spectral contents.

To better illustrate our reconstruction results and compare them to results obtained using state-of-the-art algorithms, we present separately the spatial distribution and the spectral distribution obtained for each object.

a) *Spatial distribution:* The spatial distributions are illustrated in Figs. 8, 9, and 10 by taking monochromatic images at three wavelengths, $\lambda = 6, 12, 18 \mu\text{m}$, that belong to the three spectral bands $p = 1, 4$ and 7 , respectively. The results are compared with the state-of-the-art 2D deconvolution of the images for each band described in Appendix C.

The proposed reconstructions show good performance. The dynamic range and the spatial distribution of the monochromatic images are well reconstructed with errors around 0.62% for Obj_1 , 2.20% for Obj_2 , and 5.75% for Obj_3 . This illustrates the efficiency of the proposed algorithm for reconstruction at all wavelengths. The comparison between the first three lines of Figs. 9 and 10 illustrates the striking improvement of the spatial resolution. Our algorithm correctly recovers the sharp edges and small-scale gradients contained in the original objects. Thanks to the mixing model, the spatial resolution at all wavelengths is determined by the spatial resolution of the mixing coefficients. Therefore, the reconstructed monochromatic images do not show increasing blur with increasing wavelength, unlike the images used as inputs.

Using the state-of-the-art method, the reconstruction errors are higher by significant factors (≈ 2 to 100), and the dynamic range is generally not properly restored. This is due to the integration over the wide spectral bands, and to the spectral dependence of the PSF within each band which is neglected.

b) Spectral distribution: The spectral distributions, for one spatial position, are illustrated in Fig. 11 with a comparison between the spectrum of the original object and the reconstructed ones using the proposed and the state-of-the-art algorithms. We see that the proposed algorithm produces spectra that perfectly fit the original ones for all wavelengths. This is mainly due to:

- the linear mixing model with M known spectral components which allow to disentangle the spectral information integrated within each wideband images,
- the spectral variant PSF to model the instrument response accurately, hence the observation matrix \mathbf{H} ,
- the spectral correlations between images exploited in joint reconstruction.

In contrast, the state-of-the-art method produces a poor spectral reconstruction since the spectral information within each band is completely lost.

F. Influence of the Noise Level

The reconstruction errors wrt. the noise levels are shown in Fig. 12. As expected, the proposed algorithm is sensitive to the noise with a decrease of the reconstruction errors for an increasing SNR. The reconstruction of Obj_2 and Obj_3 is very sensitive to the noise since the noise corrupts the sharp edges in the multispectral data, and make more difficult their restoration. This is less the case for Obj_1 which is dominated by a smoother spatial distribution.

V. CONCLUSION

This paper presents an efficient reconstruction method of a hyperspectral object from a set of blurred wideband images only. First, the object is modeled with a set of mixture coefficients and spectral components using a linear mixing model, with fewer components than data images. Then, a linear multi-observations forward model is derived where data images appear as the sum of 2D convolutions of mixing coefficients. The observation model preserves the spectral information of the object and accounts for the instrument behavior such as spectral-variant PSF and spectral response of the instrument. The reconstruction of the hyperspectral object is done through the estimation of the mixture coefficients.

This ill-posed problem is tackled using the regularized least square method based on convex differentiable potential and half-quadratic optimization algorithm to enforce high spatial gradient in the solution. The performance of the reconstruction algorithm is validated for three hyperspectral objects having different spatial and spectral distributions. One object is a real-like astrophysical object and two others are synthetics. The multispectral data is simulated according to the MIRI infrared imager of the JWST, and different SNR values.

The proposed algorithm estimates the mixing coefficients and compute the hyperspectral object using the linear mixing model and the spectral component dictionary. The execution time is around 20 seconds for 50 iterations on images of 256^2 size, with an actual laptop, thanks to partial implementation in the Fourier domain.

In all experiments, the relative error is below 5 % for $\text{SNR} = 30 \text{ dB}$. In addition, the reconstruction results using the proposed algorithm are very satisfactory and outperform the state-of-the-art approach. Our algorithm correctly recovers the sharp edges and small-scale gradients contained in the original objects but blurred in the data images. Thanks to this model, the spatial resolution is constant across the wavelength and fixed by spatial resolution of mixing coefficient. It also allows us to recover the spectroscopic information contained within each band.

The spectrometer's fields of view are generally much narrower than the imagers's ones. Therefore acquiring spectroscopy data is always very time consuming, if it is not impossible for extended fields. Moreover, due to instrumental progress the spectral coverage of observations become nowadays more and more extended. If the PSF and its spectral dependence are properly characterized, our proposed algorithm appears very efficient to recover the spectroscopic information contained within wideband images, and to reconstruct spectral images with identical spatial resolution at different wavelengths.

APPENDIX A COMPUTATION OF THE MULTICHANNEL QUADRATIC SOLUTION

In this section we present the computation of the multichannel quadratic solution given by

$$\underbrace{\begin{bmatrix} \hat{\mathbf{f}}^1 \\ \vdots \\ \hat{\mathbf{f}}^M \end{bmatrix}}_{\hat{\mathbf{f}}} = \underbrace{\begin{bmatrix} \mathbf{Q}^{1,1} & \dots & \mathbf{Q}^{1,M} \\ \vdots & \ddots & \vdots \\ \mathbf{Q}^{M,1} & \dots & \mathbf{Q}^{M,M} \end{bmatrix}}_{\mathbf{Q}}^{-1} \underbrace{\begin{bmatrix} \mathbf{q}^1 \\ \vdots \\ \mathbf{q}^M \end{bmatrix}}_{\mathbf{q}},$$

where $\mathbf{Q} \in \mathbb{R}^{MN_k N_l \times MN_k N_l}$ is a non-circulant block circulant matrix and $\mathbf{q} \in \mathbb{R}^{MN_k N_l}$ is a multichannel vector. The computation of $\hat{\mathbf{f}}$ relies on the inversion of the Hessian matrix \mathbf{Q} , as first exposed in [6], [47] but for multichannel image restoration. In fact, inverting \mathbf{Q} is possible by performing diagonalization of its circulant blocks $\mathbf{Q}^{i,j}$, resulting in a set of diagonal blocks $\Lambda^{i,j}$ through the transfer equation

$$\mathbf{Q}^{i,j} = \mathbf{F}^\dagger \Lambda^{i,j} \mathbf{F}, \quad i, j \in [1, \dots, M]^2, \quad (22)$$

where \mathbf{F} and \mathbf{F}^\dagger are the discrete Fourier matrix and its conjugate, respectively. This yields

$$\mathbf{Q} = \overline{\mathbf{F}}^\dagger \Lambda_Q \overline{\mathbf{F}}, \quad \text{and} \quad \mathbf{Q}^{-1} = \overline{\mathbf{F}}^\dagger \Lambda_Q^{-1} \overline{\mathbf{F}}, \quad (23)$$

with

$$\boldsymbol{\Lambda}_Q = \begin{bmatrix} \boldsymbol{\Lambda}^{1,1} & \cdots & \boldsymbol{\Lambda}^{1,M} \\ \vdots & \ddots & \vdots \\ \boldsymbol{\Lambda}^{M,1} & \cdots & \boldsymbol{\Lambda}^{M,M} \end{bmatrix}, \quad \bar{\mathbf{F}} = \begin{bmatrix} \mathbf{F} & & \\ & \ddots & \\ & & \mathbf{F} \end{bmatrix}. \quad (24)$$

The matrix $\boldsymbol{\Lambda}_Q$ is a Non-Diagonal Block Diagonal (NDBD) matrix. Thanks to the permutation matrices \mathbf{P} , the NDBD matrix can be written as

$$\boldsymbol{\Lambda}_Q = \mathbf{P} \mathbf{R} \mathbf{P}, \quad (25)$$

where $\mathbf{R} = \text{diag}(\mathbf{R}^p), p = 1, \dots, N_k N_l$ is a diagonal block non-diagonal matrix. Each block \mathbf{R}^p is an $M \times M$ full matrix, supposedly invertible, with permutations that writes

$$(\mathbf{R}^p)_{i,j} = (\boldsymbol{\Lambda}^{i,j})_{p,p} \quad (26)$$

for $i, j \in [1, \dots, M]^2$. Therefore, since the inversion of a block diagonal matrix is also a block diagonal matrix, the inverse of $\boldsymbol{\Lambda}_Q$ can be written as

$$\boldsymbol{\Upsilon} = \boldsymbol{\Lambda}_Q^{-1} = \mathbf{P}^T \mathbf{R}^{-1} \mathbf{P}^T \quad (27)$$

where $\mathbf{R}^{-1} = \text{diag}((\mathbf{R}^p)^{-1})$, and $\boldsymbol{\Upsilon}$ is also a NDBD matrix, having a diagonal block $\boldsymbol{\Upsilon}^{i,j}$ given by

$$(\boldsymbol{\Upsilon}^{i,j})_{p,p} = ((\mathbf{R}^p)^{-1})_{i,j}. \quad (28)$$

Thanks to such properties, the multichannel quadratic solution can be computed with the DFT and $N_k N_l$ inversions of square matrices of size M . In the context of this work, $N_k N_l$ are the number of pixels and M is the number of spectral components. In addition, each block \mathbf{R}^p can be inverted in parallel. Finally, $\hat{\mathbf{f}}$ is computed just by applying the matrix $\boldsymbol{\Upsilon}$ as

$$\hat{\mathbf{f}} = \bar{\mathbf{F}}^\dagger \boldsymbol{\Lambda}_Q^{-1} \mathring{\mathbf{q}} = \bar{\mathbf{F}}^\dagger \boldsymbol{\Upsilon} \bar{\mathbf{F}} \mathbf{q} \quad (29)$$

with $\mathring{\mathbf{q}} = \bar{\mathbf{F}} \mathbf{q}$.

APPENDIX B UPDATE OF THE AUXILIARY VARIABLES

The update of all auxiliary variables is independent. The solution is given by the minimization

$$\hat{\mathbf{b}}^m = \underset{\mathbf{b}^m}{\operatorname{argmin}} \underbrace{\frac{1}{2} \left([\mathbf{D} \mathbf{f}^m]_{k,l} - [\mathbf{b}^m]_{k,l} \right)^2}_{\psi([\mathbf{b}^m]_{k,l})} + \xi \left([\mathbf{b}^m]_{k,l} \right)$$

where ψ is a convex and differentiable and separable function with respect to the minimizer. Since the criterion is convex differentiable, a sufficient condition is $\psi' \left(\hat{\mathbf{b}}^m \right)_{k,l} = 0, \forall k \in [1, N_k] \text{ and } \forall l \in [1, N_l]$. The derivative function ψ' is computed by substituting the auxiliary function (associated to Huber function in (10)) in ψ . This yields

$$\psi' \left(\widehat{\mathbf{b}}^m \right)_{k,l} = \begin{cases} \left(\widehat{\mathbf{b}}^m \right)_{k,l} - [\mathbf{Df}^m]_{k,l} + \frac{2a}{1-2a} \left[\widehat{\mathbf{b}}^m \right]_{k,l}, & \text{If } \left| \left[\widehat{\mathbf{b}}^m \right]_{k,l} \right| < (1-2a)s, \\ \left(\widehat{\mathbf{b}}^m \right)_{k,l} - [\mathbf{Df}^m]_{k,l} + a 2s \operatorname{sign} \left(\left[\widehat{\mathbf{b}}^m \right]_{k,l} \right), & \text{Otherwise.} \end{cases}$$

Thus, the obtained auxiliary variables are

$$\begin{aligned} \left[\widehat{\mathbf{b}}^m \right]_{k,l} &= \begin{cases} [\mathbf{Df}^m]_{k,l} - 2a [\mathbf{Df}^m]_{k,l}, & \text{If } \left| [\mathbf{Df}^m]_{k,l} \right| < s, \\ [\mathbf{Df}^m]_{k,l} - a 2s \operatorname{sign} \left([\mathbf{Df}^m]_{k,l} \right), & \text{Otherwise.} \end{cases} \\ &= [\mathbf{Df}^m]_{k,l} - a \varphi' \left([\mathbf{Df}^m]_{k,l} \right). \end{aligned} \quad (30)$$

Finally, we obtain

$$\widehat{\mathbf{b}} = \mathbf{Df} - a \varphi' \left(\overline{\mathbf{Df}} \right) \quad (31)$$

where φ' is the first derivative of Huber function and it is given by

$$\varphi'(x) = \begin{cases} 2x & \text{if } |x| < s \\ 2s \operatorname{sign}(x) & \text{otherwise} \end{cases} = 2x \min \left(1, \frac{s}{|x|} \right).$$

APPENDIX C

STATE-OF-THE-ART METHOD FOR HYPERSPECTRAL RECONSTRUCTION: 2D DECONVOLUTION

As mentioned in Section I, the state-of the-art method for reconstruction consists of a 2D deconvolution of the images for each band with the associated broadband PSF. We compute for each band the spectral-invariant broadband PSF as the sum of monochromatic PSFs weighted by the spectral response of the instrument (see Fig. 2) and the object spectrum which is assumed to be constant over the field-of-view of the imager:

$$h_{\text{broad}}(x, y) = \frac{\int_{\mathbb{R}_+} \omega(\lambda) s(\lambda) h(x, y, \lambda) d\lambda}{\int_{\mathbb{R}_+} \omega(\lambda) s(\lambda) d\lambda}. \quad (32)$$

The object spectrum is generally not known, so we take a flat spectrum. In addition, we implement an unsupervised image deconvolution method [48] by considering a quadratic regularization.

ACKNOWLEDGMENT

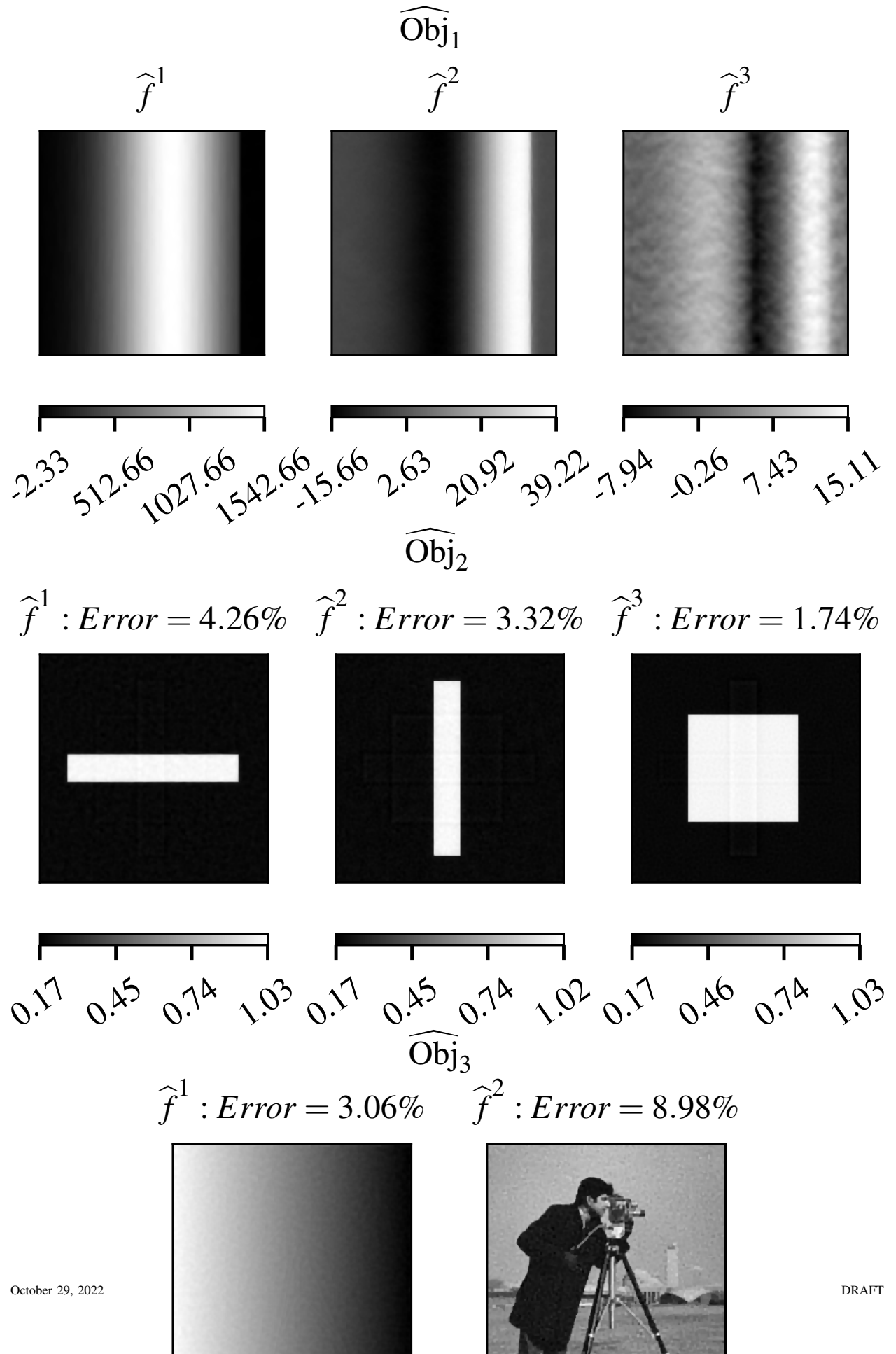
The authors would like to thank Nathalie Ysard for kindly providing the simulation of the hyperspectral object *HorseHead*.

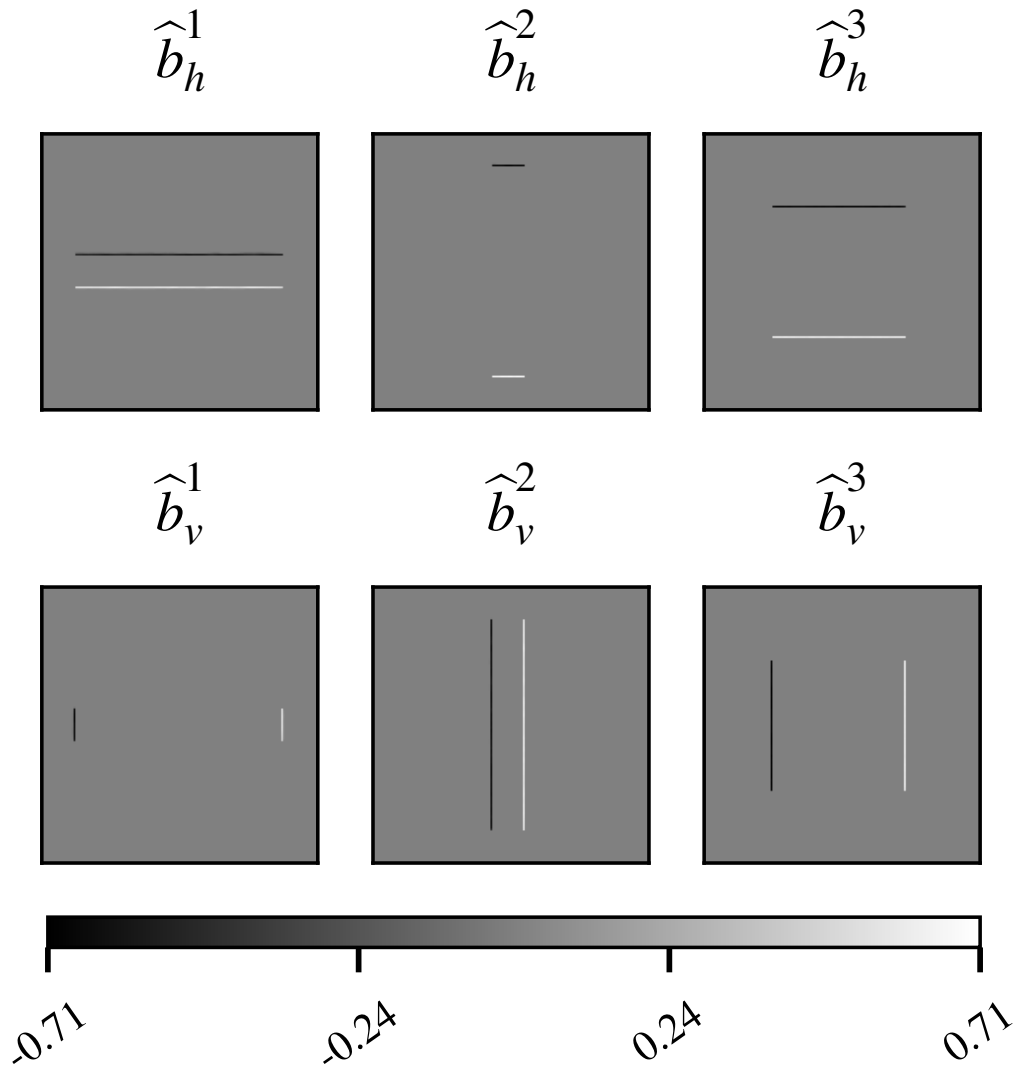
REFERENCES

- [1] R. Lionello, J. A. Linker, and Z. Mikić, “Multispectral emission of the sun during the first whole sun month: Magnetohydrodynamic simulations,” *The Astrophysical Journal*, vol. 690, no. 1, p. 902, 2008.
- [2] D. A. Landgrebe, *Signal theory methods in multispectral remote sensing*. John Wiley & Sons, 2005, vol. 29.

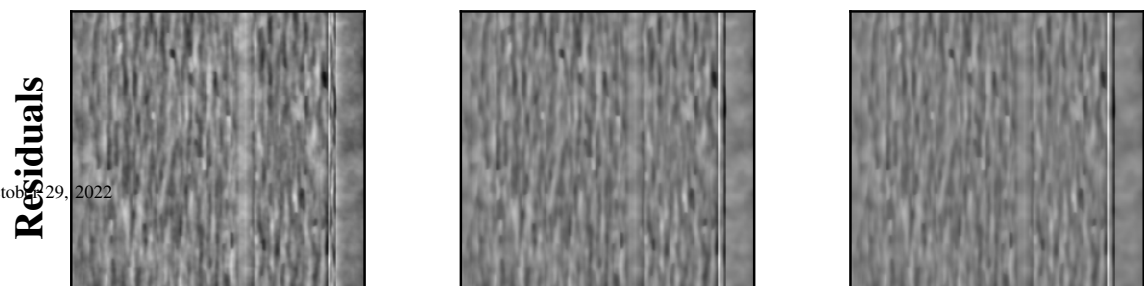
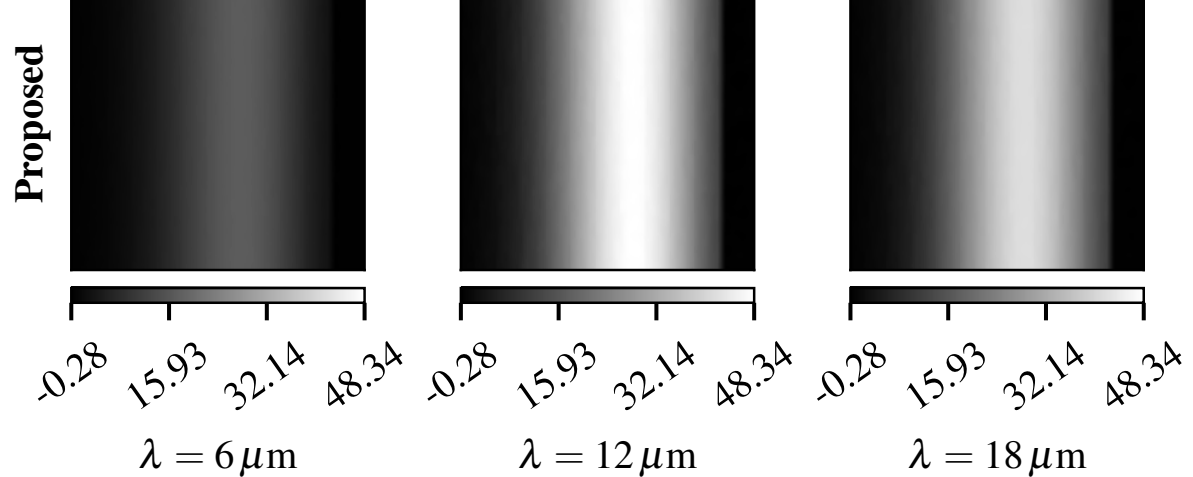
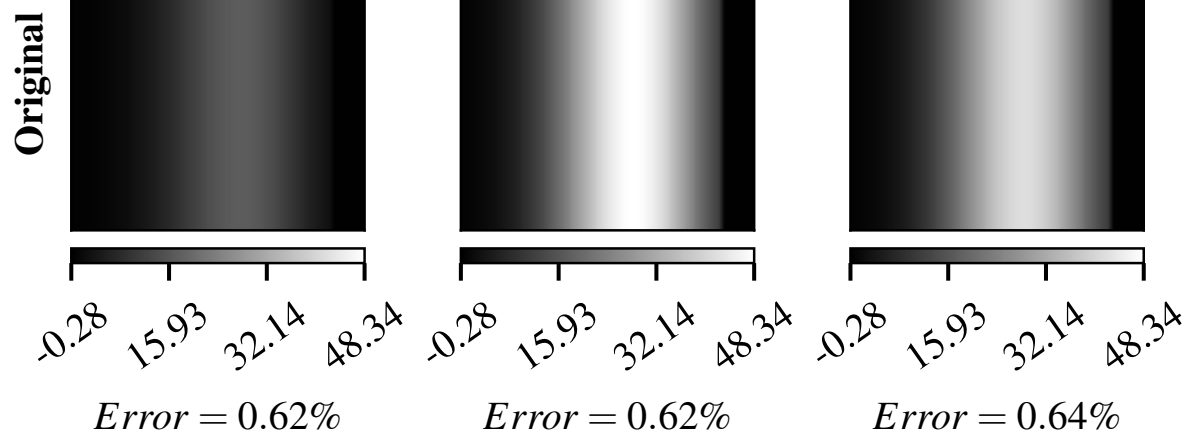
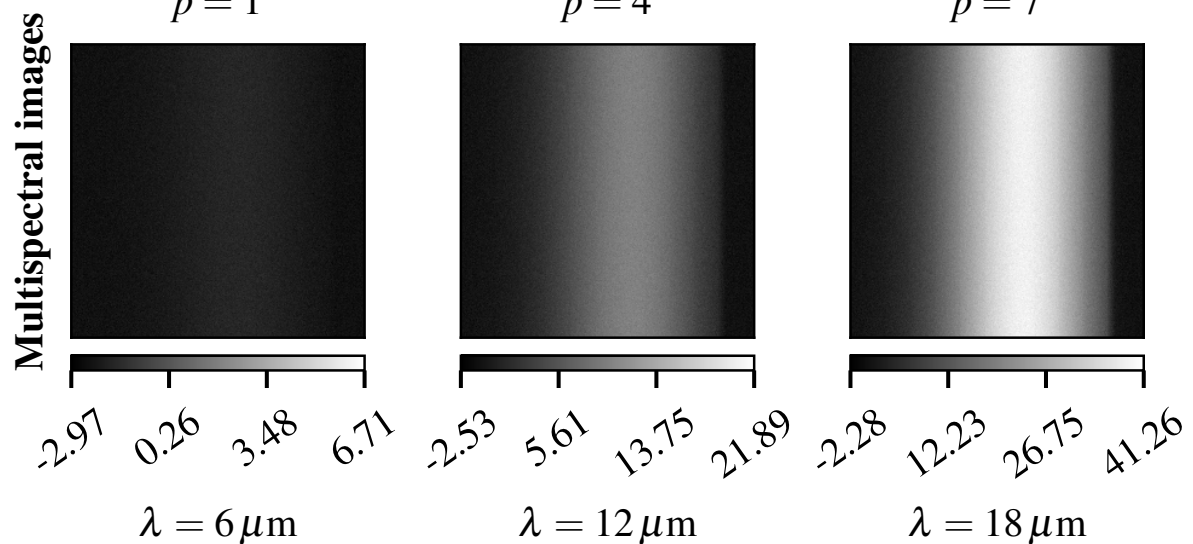
- [3] T. O. McBride, B. W. Pogue, S. Poplack, S. Soho, W. A. Wells, S. Jiang, K. D. Paulsen *et al.*, "Multispectral near-infrared tomography: a case study in compensating for water and lipid content in hemoglobin imaging of the breast," *Journal of biomedical optics*, vol. 7, no. 1, pp. 72–79, 2002.
- [4] M. Dickinson, G. Bearman, S. Tille, R. Lansford, and S. Fraser, "Multi-spectral imaging and linear unmixing add a whole new dimension to laser scanning fluorescence microscopy," *Biotechniques*, vol. 31, no. 6, pp. 1272–1279, 2001.
- [5] P. Guillard, T. Rodet, S. Ronayette, J. Amiaux, A. Abergel, V. Moreau, J. Augueres, A. Bensalem, T. Orduna, C. Nehmé *et al.*, "Optical performance of the jwst/miri flight model: characterization of the point spread function at high resolution," in *SPIE Astronomical Telescopes+ Instrumentation*. International Society for Optics and Photonics, 2010, pp. 77310J–77310J.
- [6] N. P. Galatsanos and R. T. Chin, "Digital restoration of multichannel images," *IEEE Transactions on Acoustics, Speech, and Signal Processing*, vol. 37, no. 3, pp. 415–421, 1989.
- [7] L. Denis, É. Thiébaut, and F. Soulez, "Fast model of space-variant blurring and its application to deconvolution in astronomy," in *Image Processing (ICIP), 2011 18th IEEE International Conference on*. IEEE, 2011, pp. 2817–2820.
- [8] É. Thiébaut, L. Dénis, F. Soulez, and R. Mourya, "Spatially variant psf modeling and image deblurring," in *SPIE Astronomical Telescopes+ Instrumentation*. International Society for Optics and Photonics, 2016, pp. 99097N–99097N.
- [9] G. Aniano, B. Draine, K. Gordon, and K. Sandstrom, "Common-resolution convolution kernels for space-and ground-based telescopes," *Publications of the Astronomical Society of the Pacific*, vol. 123, no. 908, p. 1218, 2011.
- [10] A. Boucaud, M. Bocchio, A. Abergel, F. Orieux, H. Dole, and M. A. Hadj-Youcef, "Convolution kernels for multi-wavelength imaging," *Astronomy & Astrophysics*, vol. 596, p. A63, 2016.
- [11] M. A. Hadj-Youcef, F. Orieux, A. Fraysse, and A. Abergel, "Spatio-spectral multichannel reconstruction from few low-resolution multispectral data," in *2018 26th European Signal Processing Conference (EUSIPCO)*, Sep 2018.
- [12] N. Keshava and J. F. Mustard, "Spectral unmixing," *IEEE signal processing magazine*, vol. 19, no. 1, pp. 44–57, 2002.
- [13] A. Plaza, P. Martínez, R. Pérez, and J. Plaza, "A quantitative and comparative analysis of endmember extraction algorithms from hyperspectral data," *IEEE transactions on geoscience and remote sensing*, vol. 42, no. 3, pp. 650–663, 2004.
- [14] J. M. Bioucas-Dias, A. Plaza, N. Dobigeon, M. Parente, Q. Du, P. Gader, and J. Chanussot, "Hyperspectral unmixing overview: Geometrical, statistical, and sparse regression-based approaches," *IEEE journal of selected topics in applied earth observations and remote sensing*, vol. 5, no. 2, pp. 354–379, 2012.
- [15] J. B. Adams, M. O. Smith, and P. E. Johnson, "Spectral mixture modeling: A new analysis of rock and soil types at the viking lander 1 site," *Journal of Geophysical Research: Solid Earth*, vol. 91, no. B8, pp. 8098–8112, 1986.
- [16] J. Settle and N. Drake, "Linear mixing and the estimation of ground cover proportions," *International Journal of Remote Sensing*, vol. 14, no. 6, pp. 1159–1177, 1993.
- [17] V. Haertel and Y. E. Shimabukuro, "Spectral linear mixing model in low spatial resolution image data," in *Geoscience and Remote Sensing Symposium, 2004. IGARSS'04. Proceedings. 2004 IEEE International*, vol. 4. IEEE, 2004, pp. 2546–2549.
- [18] O. Berne, C. Joblin, Y. Deville, J. Smith, M. Rapacioli, J. Bernard, J. Thomas, W. Reach, and A. Abergel, "Analysis of the emission of very small dust particles from spitzer spectro-imagery data using blind signal separation methods," *Astronomy & Astrophysics*, vol. 469, no. 2, pp. 575–586, 2007.
- [19] Y. Tarabalka, J. A. Benediktsson, and J. Chanussot, "Spectral–spatial classification of hyperspectral imagery based on partitional clustering techniques," *IEEE Transactions on Geoscience and Remote Sensing*, vol. 47, no. 8, pp. 2973–2987, 2009.
- [20] Z. Guo, T. Wittman, and S. Osher, "L1 unmixing and its application to hyperspectral image enhancement," in *Algorithms and Technologies for Multispectral, Hyperspectral, and Ultraspectral Imagery XV*, vol. 7334. International Society for Optics and Photonics, 2009, p. 73341M.
- [21] N. Dobigeon, S. Moussaoui, M. Coulon, J.-Y. Tourneret, and A. O. Hero, "Joint bayesian endmember extraction and linear unmixing for hyperspectral imagery," *IEEE Transactions on Signal Processing*, vol. 57, no. 11, pp. 4355–4368, 2009.
- [22] L. Loncan, L. B. Almeida, J. M. Bioucas-Dias, X. Briottet, J. Chanussot, N. Dobigeon, S. Fabre, W. Liao, G. A. Licciardi, M. Simoes *et al.*, "Hyperspectral pansharpening: A review," *arXiv preprint arXiv:1504.04531*, 2015.
- [23] G. Demont, "Image reconstruction and restoration: Overview of common estimation structures and problems," *IEEE Transactions on Acoustics, Speech, and Signal Processing*, vol. 37, no. 12, pp. 2024–2036, 1989.
- [24] P. Bouchet, M. García-Marín, P.-O. Lagage, J. Amiaux, J.-L. Auguéres, E. Bauwens, J. Blommaert, C. Chen, Ö. Detre, D. Dicken *et al.*, "The Mid-Infrared Instrument for the James Webb Space Telescope, III: MIRIM, The MIRI Imager," *Publications of the Astronomical Society of the Pacific*, vol. 127, no. 953, p. 612, 2015.

- [25] J. P. Gardner, J. C. Mather, M. Clampin, R. Doyon, M. A. Greenhouse, H. B. Hammel, J. B. Hutchings, P. Jakobsen, S. J. Lilly, K. S. Long *et al.*, “The james webb space telescope,” *Space Science Reviews*, vol. 123, no. 4, pp. 485–606, 2006.
- [26] J. W. Goodman, *Introduction to Fourier optics*. Roberts and Company Publishers, 2005.
- [27] S. Bongard, F. Soulez, É. Thiébaut, and É. Pecontal, “3d deconvolution of hyper-spectral astronomical data,” *Monthly Notices of the Royal Astronomical Society*, vol. 418, no. 1, pp. 258–270, 2011.
- [28] B. Hunt, “A matrix theory proof of the discrete convolution theorem,” *IEEE Transactions on Audio and Electroacoustics*, vol. 19, no. 4, pp. 285–288, 1971.
- [29] A. N. Tikhonov, A. Goncharsky, V. Stepanov, and A. G. Yagola, *Numerical methods for the solution of ill-posed problems*. Springer Science & Business Media, 2013, vol. 328.
- [30] L. I. Rudin, S. Osher, and E. Fatemi, “Nonlinear total variation based noise removal algorithms,” *Physica D: Nonlinear Phenomena*, vol. 60, no. 1, pp. 259–268, 1992.
- [31] I. Daubechies and G. Teschke, “Wavelet based image decomposition by variational functionals,” in *Proc. SPIE Vol*, vol. 5266, 2004, pp. 94–105.
- [32] M. A. Figueiredo and R. D. Nowak, “An em algorithm for wavelet-based image restoration,” *IEEE Transactions on Image Processing*, vol. 12, no. 8, pp. 906–916, 2003.
- [33] D. Geman and G. Reynolds, “Constrained restoration and the recovery of discontinuities,” *IEEE Transactions on pattern analysis and machine intelligence*, vol. 14, no. 3, pp. 367–383, 1992.
- [34] D. Geman and C. Yang, “Nonlinear image recovery with half-quadratic regularization,” *IEEE Transactions on Image Processing*, vol. 4, no. 7, pp. 932–946, 1995.
- [35] P. Perona and J. Malik, “Scale-space and edge detection using anisotropic diffusion,” *IEEE Transactions on pattern analysis and machine intelligence*, vol. 12, no. 7, pp. 629–639, 1990.
- [36] A. Chambolle, “An algorithm for total variation minimization and applications,” *Journal of Mathematical imaging and vision*, vol. 20, no. 1-2, pp. 89–97, 2004.
- [37] P. Charbonnier, L. Blanc-Féraud, G. Aubert, and M. Barlaud, “Deterministic edge-preserving regularization in computed imaging,” *IEEE Transactions on image processing*, vol. 6, no. 2, pp. 298–311, 1997.
- [38] J. Idier, “Convex half-quadratic criteria and interacting auxiliary variables for image restoration,” *IEEE Transactions on Image Processing*, vol. 10, no. 7, pp. 1001–1009, 2001.
- [39] N. P. Galatsanos, A. K. Katsaggelos, R. T. Chin, and A. D. Hillery, “Least squares restoration of multichannel images,” *IEEE Transactions on Signal Processing*, vol. 39, no. 10, pp. 2222–2236, 1991.
- [40] M. D. Perrin, R. Soummer, E. M. Elliott, M. D. Lallo, and A. Sivaramakrishnan, “Simulating point spread functions for the james webb space telescope with webbpsf,” in *Space Telescopes and Instrumentation 2012: Optical, Infrared, and Millimeter Wave*, vol. 8442. International Society for Optics and Photonics, 2012, p. 84423D.
- [41] M. D. Perrin, A. Sivaramakrishnan, C.-P. Lajoie, E. Elliott, L. Pueyo, S. Ravindranath, and L. Albert, “Updated point spread function simulations for jwst with webbpsf,” in *Space Telescopes and Instrumentation 2014: Optical, Infrared, and Millimeter Wave*, vol. 9143. International Society for Optics and Photonics, 2014, p. 91433X.
- [42] A. Glasse, G. Rieke, E. Bauwens, M. García-Marín, M. Ressler, S. Rost, T. V. Tikkanen, B. Vandebussche, and G. Wright, “The Mid-Infrared Instrument for the James Webb Space Telescope, IX: Predicted Sensitivity,” *Publications of the Astronomical Society of the Pacific*, vol. 127, no. 953, p. 686, 2015.
- [43] U. of Arizona, “Table of integration window for each filter,” 2018, accessed 2018-31-10. [Online]. Available: http://ircamera.as.arizona.edu/MIR/ImPCE_TN-00072-ATC-Iss2.xlsx
- [44] A. Abergel, D. Teyssier, J. Bernard, F. Boulanger, A. Coulais, D. Fosse, E. Falgarone, M. Gerin, M. Perault, J.-L. Puget *et al.*, “Isocam and molecular observations of the edge of the horsehead nebula,” *Astronomy & Astrophysics*, vol. 410, no. 2, pp. 577–585, 2003.
- [45] I. T. Jolliffe, “Principal component analysis and factor analysis,” in *Principal component analysis*. Springer, 1986, pp. 115–128.
- [46] D. D. Lee and H. S. Seung, “Algorithms for non-negative matrix factorization,” in *Advances in neural information processing systems*, 2001, pp. 556–562.
- [47] N. P. Galatsanos, M. N. Wernick, A. K. Katsaggelos, and R. Molina, “Multichannel image recovery,” *Handbook of Image and Video Processing*, vol. 12, pp. 155–168, 2000.
- [48] F. Orieux, J.-F. Giovannelli, and T. Rodet, “Bayesian estimation of regularization and point spread function parameters for wiener–hunt deconvolution,” *JOSA A*, vol. 27, no. 7, pp. 1593–1607, 2010.

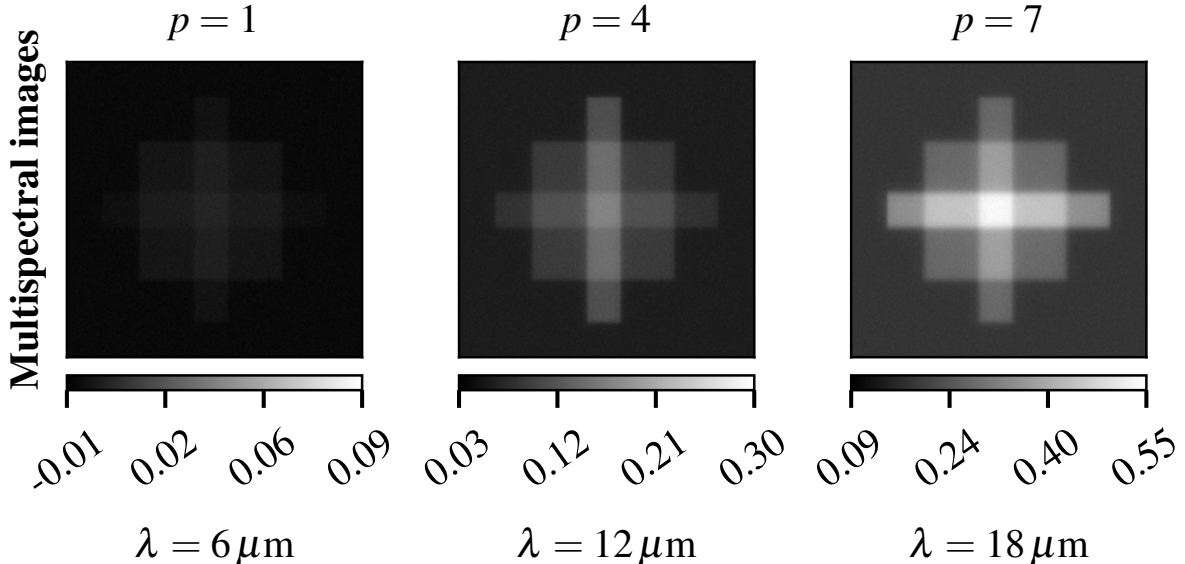


Fig. 7. Estimated auxiliary variables, horizontal and vertical, for $\widehat{\text{Obj}}_2$.

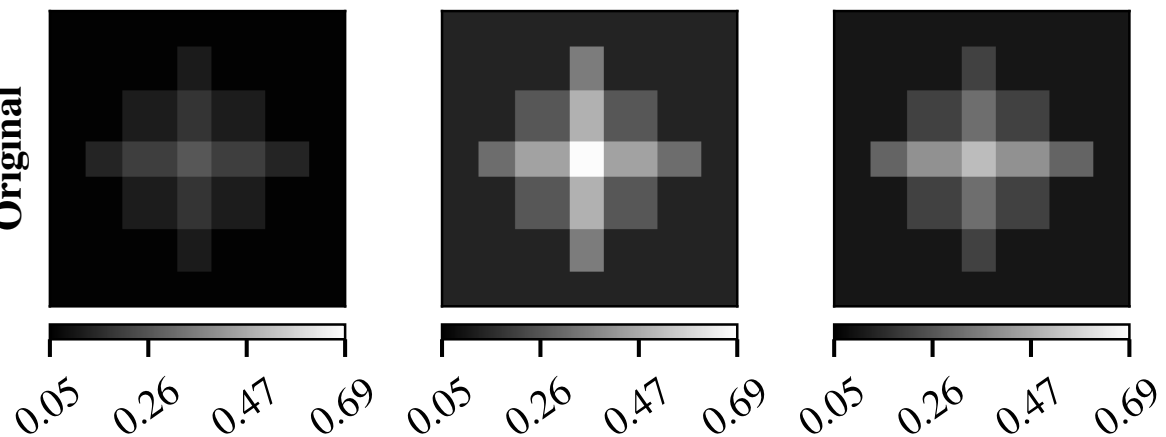
$p = 1 \quad p = 4 \quad p = 7$



$p = 1 \quad p = 4 \quad p = 7$

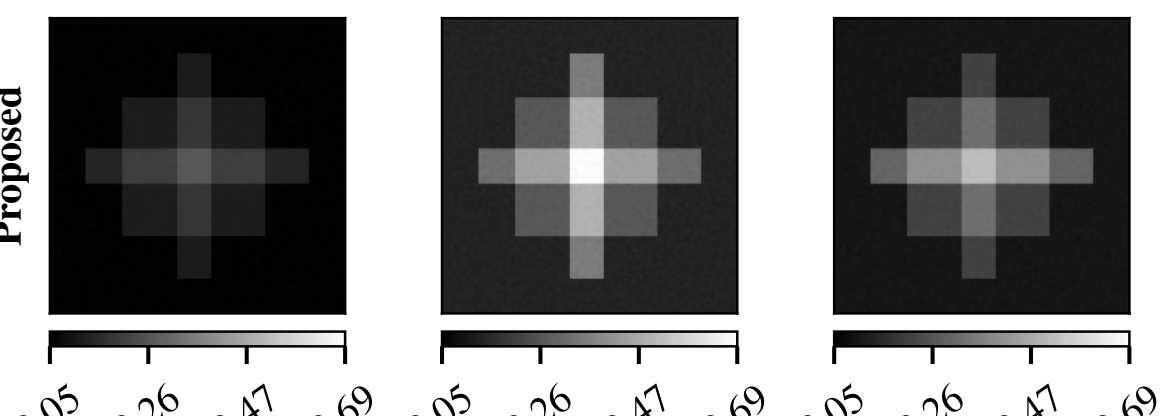


Original



Error = 2.15%

Proposed

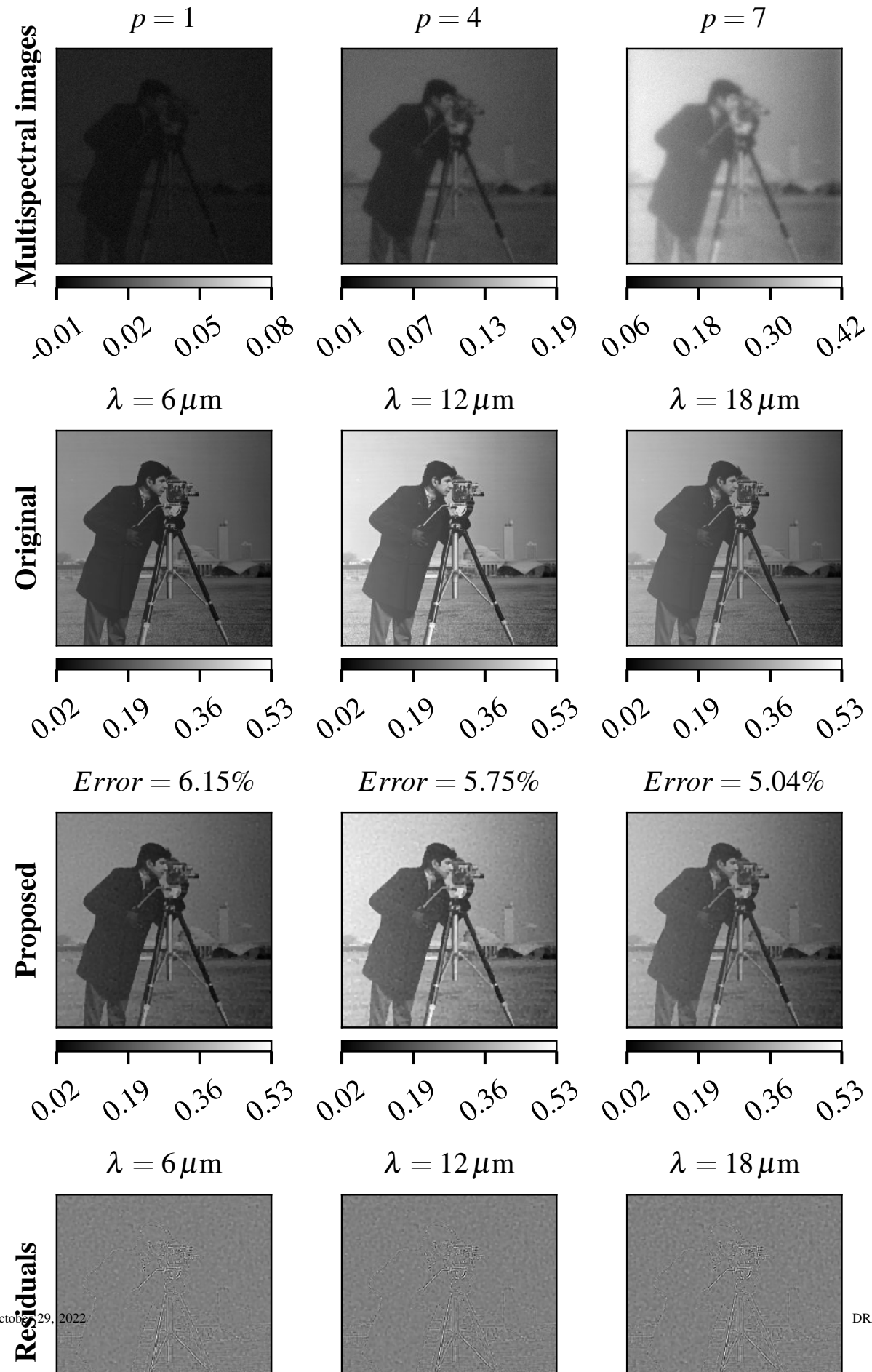


$\lambda = 6\mu\text{m}$

$\lambda = 12\mu\text{m}$

$\lambda = 18\mu\text{m}$

Residuals



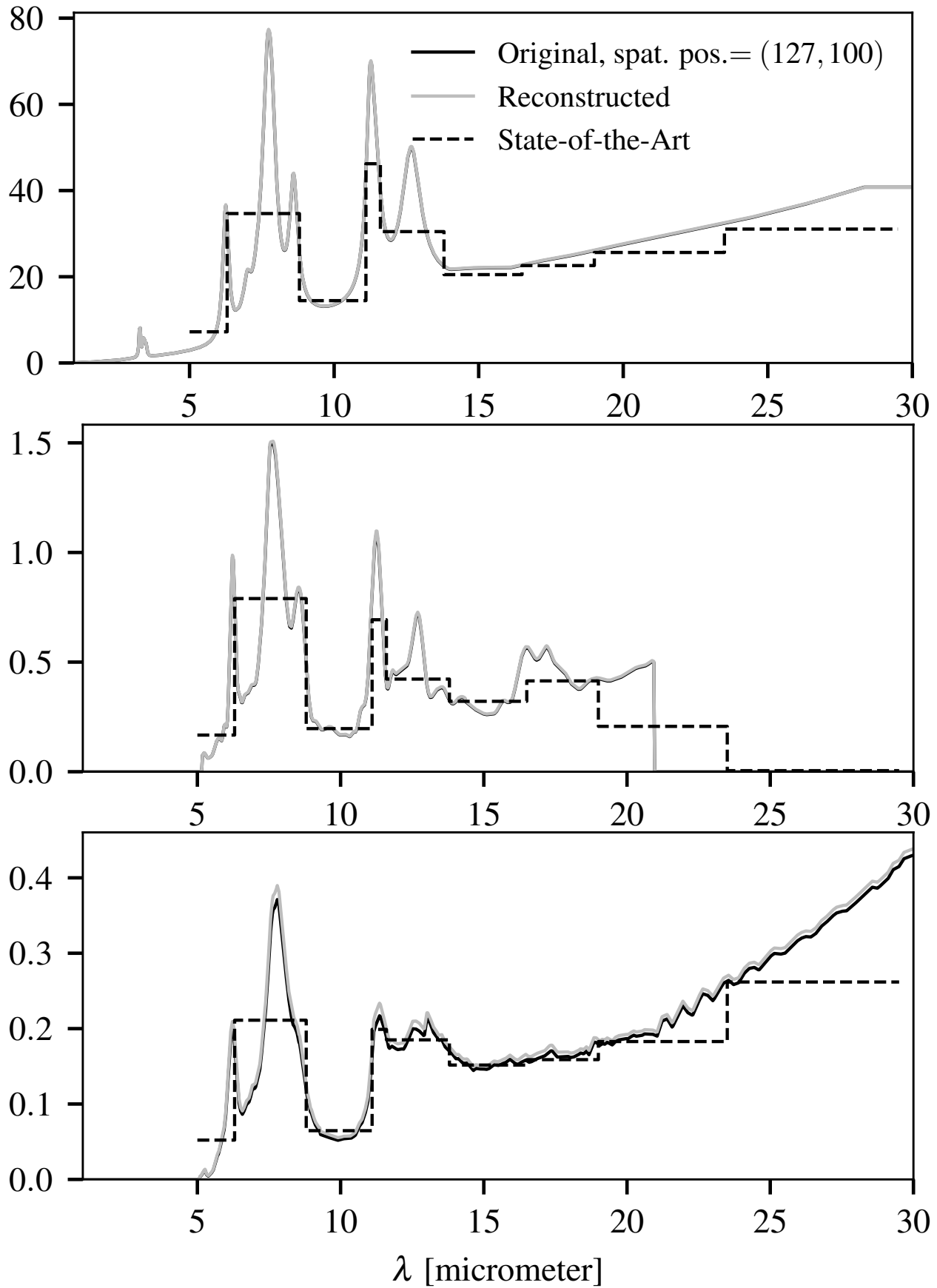


Fig. 11. Spectral distribution of the reconstruction results for one spatial position (127,100) for Obj₁ (top), Obj₂ (middle) and Obj₃ (bottom).

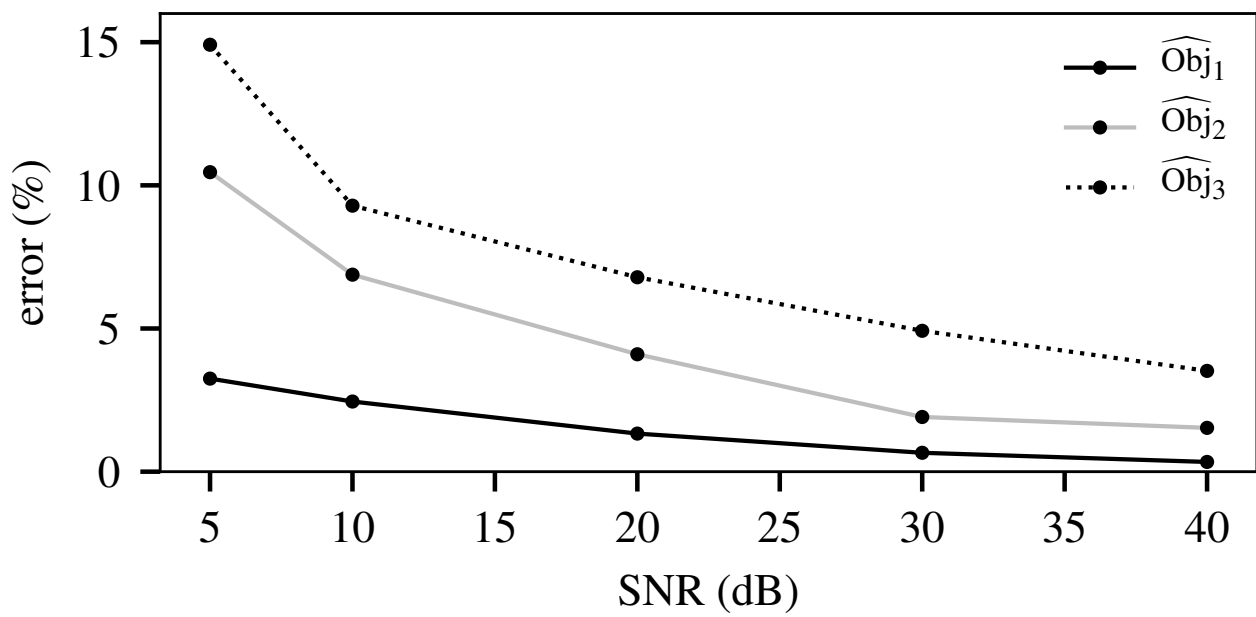


Fig. 12. Influence of the SNR on the reconstruction.